

FAITHFULNESS UNDER THE DISTRIBUTION: A NEW LOOK AT ATTRIBUTION EVALUATION

Anonymous authors

Paper under double-blind review

ABSTRACT

Evaluating the faithfulness of attribution methods remains an open challenge. Standard metrics such as Insertion and Deletion Scores rely on heuristic input perturbations (e.g., zeroing pixels), which often push samples out of the data distribution (OOD). This can distort model behavior and lead to unreliable evaluations. We propose FUD, a novel evaluation framework that reconstructs masked regions using score-based diffusion models to produce in-distribution, semantically coherent inputs. This distribution-aware approach avoids the common pitfalls of existing Attribution Evaluation Methods (AEMs) and yields assessments that more accurately reflect attribution faithfulness. Experiments across models show that FUD produces significantly different—and more reliable—judgments than prior approaches. Our implementation is available at: <https://anonymous.4open.science/r/FUD-CCD5/>.

1 INTRODUCTION

With the widespread adoption of deep learning techniques in critical domains such as medical diagnosis (Bakator & Radosav, 2018), financial risk control (Mashrur et al., 2020), autonomous driving (Grigorescu et al., 2020), and security surveillance (Yu et al., 2021), the issue of model interpretability has attracted increasing attention. Although deep neural networks have achieved breakthrough performance across a range of tasks, their complex internal mechanisms are often regarded as a “black box,” making it difficult to understand the rationale behind specific predictions. In safety-critical or high-risk applications, a lack of reasonable explanation for model decisions may lead to severe consequences (Van der Velden et al., 2022). Therefore, enhancing model interpretability not only helps to foster user trust, but also facilitates error analysis, model debugging, and even improves robustness and generalization performance.

Among the various explainability techniques, attribution methods have emerged as a crucial approach for interpreting complex models by mapping prediction outcomes back to the input space (such as image pixels or feature dimensions) to identify key regions or factors that the model focuses on. These methods are widely employed in tasks like image classification (Rao et al., 2022) and sentiment analysis (Pan et al., 2024), and have demonstrated significant value, particularly in scenarios that demand high levels of security in model decision-making.

However, attribution methods themselves are not always reliable or consistent, as different techniques may produce significantly divergent explanations for the same model prediction. Therefore, how to objectively assess the quality of attribution results has emerged as a core challenge in current research. Faithfulness (Petsiuk et al., 2018; Yeh et al., 2019) is widely regarded as a key criterion for evaluating the effectiveness of attribution methods. Such criterion reflects the consistency between the attribution results and the actual decision-making basis of the model: a highly faithful attribution method indicates that the highlighted high-contribution regions genuinely play a critical role in the model’s prediction. In other words, when these regions are removed or perturbed, the model’s output changes significantly.

Building on this insight, the research community has proposed various quantitative metrics to assess faithfulness. Among them, the most representative and widely adopted are the Insertion & Deletion Scores (Petsiuk et al., 2018) and Infidelity (Yeh et al., 2019). The Insertion & Deletion Score is a pair of complementary evaluation metrics, which start from the “substitutability of contribution areas” and simulate the way humans understand the model’s dependent areas. Specifically, the Deletion Score progressively removes the highest-scoring regions from the original input—i.e., the pixels or features

054
055
056
057
058
059
060
061
062
063
064
065
066
067
068
069
070
071
072
073
074
075
076
077
078
079
080
081
082
083
084
085
086
087
088
089
090
091
092
093
094
095
096
097
098
099
100
101
102
103
104
105
106
107

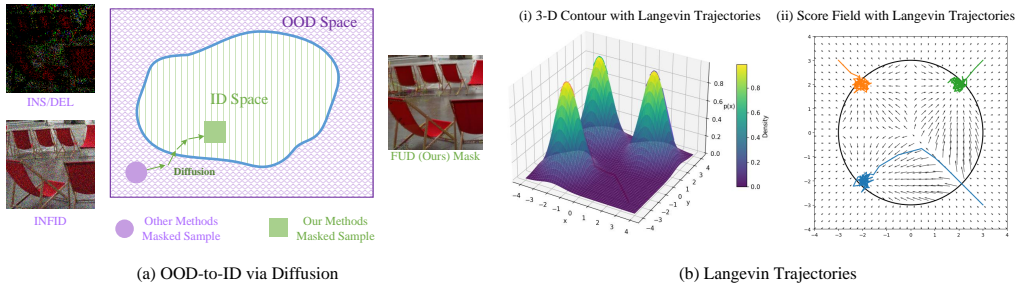


Figure 1: **Overview of the FUD framework.** (a) The left panel illustrates the core motivation of FUD: compared to conventional attribution evaluation metrics such as *INS/DEL* and *INFID*, which generate perturbed inputs drifting into the OOD space (purple area), FUD ensures that evaluation samples remain within the ID manifold (green area) by reconstructing masked regions via a score-based diffusion model. (b) The right panel shows how FUD leverages Langevin dynamics to guide inputs back toward the data manifold. Subfigure (i) visualizes Langevin trajectories in a toy 3D density; subfigure (ii) shows how the learned score field $\nabla_x \log p_\theta(x)$ steers samples from OOD to ID regions. The derivation of this score function is discussed in Section 3.3.

with the largest attribution values—and records the corresponding changes in the model’s output at each step. In contrast, the Insertion Score starts from a blank image (such as an all-zero input or a blurred background) and gradually inserts the highest-scoring regions from the attribution map in order of decreasing attribution value.

Infidelity is another faithfulness metric based on expected values, focusing on the explanatory power of attribution scores with respect to prediction changes. It is defined as the mean squared error between the attribution values and the actual changes in the model’s predictions under a set of input perturbations, such as additive noise. Although existing Attribution Evaluation Methods (AEMs) provide powerful tools for quantitatively analyzing attribution methods, they also suffer from notable limitations. These methods fundamentally rely on the core operation of feature removal or modification, a process that inherently introduces two key heuristic mistakes, **introducing additional information** and **being affected by the instability of the out-of-distribution space of models**. We will discuss the details later. As a result, mainstream attribution methods often fail to faithfully reflect the true decision-making basis of the model, leading to explanations that lack faithfulness. To address the shortcomings of current AEMs in accurately capturing the faithfulness of attribution algorithms, inspired by Score-based Generative Modeling (SGM), we propose a new evaluation method called FUD. FUD is capable of constructing attribution evaluation samples that remain within the data distribution while preserving the essential information required for faithful evaluation. The core idea of FUD lies in its ability to leverage the score function learned from the true data distribution to pull out-of-distribution samples back into the data manifold, while simultaneously preserving the critical information needed for faithful attribution evaluation. Building on this idea, we present a detailed derivation of the distributional formulation underlying FUD. It is worth emphasizing that FUD can be readily applied by incorporating the target model into an existing score function, without the need for any additional training. An overview of the proposed pipeline is shown in Fig. 1.

Contributions. (1) we first identify that existing widely used Attribution Evaluation Methods (AEMs) universally suffer from significant heuristic mistakes systematically exhibit significant heuristic issues, posing substantial risks to explainable AI, and we analyse these issues from a distributional perspective using explicit OOD detection and image quality metrics; (2) we propose and formally derive the FUD evaluation method, explicitly designed to avoid these mistakes heuristic pitfalls, and validate its effectiveness through extensive experiments across diverse use cases; and (3) we release FUD as an open-source toolkit to promote transparency, reproducibility, and community engagement.

2 RELATED WORK

Attribution methods aim to explain model predictions by identifying input regions most responsible for the output, with approaches such as Integrated Gradients (IG) (Sundararajan et al., 2017), Guided IG (Kapishnikov et al., 2021), Boundary-based IG (Wang et al., 2021), and adversarial-path methods including AGI (Pan et al., 2021) and subsequent adversarial attribution variants (Zhu et al., 2024b;a;c). Evaluating attribution faithfulness typically relies on perturbation-based metrics such as Insertion & Deletion Scores (Petsiuk et al., 2018), Infidelity (Yeh et al., 2019), Sensitivity- n (Ancona et al., 2017), and optimized-mask approaches (Fong & Vedaldi, 2017; Fong et al., 2019), all of which introduce distribution shifts to varying degrees. In addition, generative in-filling approaches (Chang et al., 2019; Agarwal & Nguyen, 2020) use learned generative models to replace removed pixels with realistic content; however, they do not incorporate classifier-input gradients and may inadvertently introduce class-supporting evidence instead of faithfully removing it. These methods collectively highlight the trade-off between interpretability and distributional consistency, motivating more robust evaluation frameworks. A detailed and extended discussion of attribution methods and evaluation metrics is provided in Appendix A.

3 METHOD

3.1 PROBLEM DEFINITION

In the Research of interpretability for deep learning models, attribution methods aim to measure the contribution of input features to the model’s decision. Given a trained predictive model $f(x)$, where $x \in \mathbb{R}^n$ represents an n -dimensional input sample, the model’s output is a c -dimensional vector $f(x) \in \mathbb{R}^c$, corresponding to the probability distribution or prediction scores over c classes. Attribution methods attempt to generate an interpretable representation $A(x) \in \mathbb{R}^n$ for the input sample x , indicating the importance of each input feature or feature region for the model output (usually for a specific class). For the i -th feature in the image, a larger value of $A(x)_i$ represents a greater contribution of that feature to the model’s decision. In the Appendix A, we also provide a detailed related work of the current state-of-the-art attribution methods and commonly used AEMs.

Model-centric out-of-distribution (OOD) definition. Throughout this paper, OOD is defined with respect to the original model under evaluation. That is, a perturbed sample is considered in-distribution if it lies on (or near) the model’s learned data manifold, regardless of whether it appears visually “natural” to humans. This model-centric view is consistent with our goal—assessing attribution faithfulness for the original model—rather than for a re-trained or adaptively fine-tuned model. See Appx. F for objective OOD-detection evidence supporting this distinction.

3.2 THE HEURISTIC MISTAKES OF CURRENT AEMs

Most of the currently designed AEMs (Petsiuk et al., 2018; Yeh et al., 2019; Ancona et al., 2017) are heuristic in nature. Although they are often supported by some mathematical interpretations and theoretical foundations (Yeh et al., 2019), they are essentially based on intuition-driven designs. Of course, we do not consider heuristic or intuition-driven evaluation method design to be a wrong choice. Just as using the probability output of a classification model as a measure of confidence is widely accepted—it effectively reflects the relative likelihoods of different class decisions made by the model. Since AEMs require an understanding of the model’s internal mechanisms, and such understanding still largely relies on heuristic reasoning and empirical analysis, we inevitably make reasonable assumptions about these internal processes during interpretation. However, because these assumptions are themselves heuristic, it is difficult to design AEMs based on first principles. But precisely because of this, we need to approach the potential heuristic mistakes with greater rigor.

We find that mainstream AEMs commonly involve feature insertion and deletion during their design. For example, the insertion score is calculated by progressively inserting features based on their attribution-estimated contribution values in descending order, and observing the increase in the confidence score of the target class. A higher insertion score indicates that the attribution method has successfully identified important, high-contribution features. Similarly, the deletion score involves removing features in descending order of their estimated contribution values, where a lower score indicates a better attribution method. During this process, a corresponding mask $M \in \{0, 1\}^n$ is

generated, where the ratio of 0 and 1 depends on the number of features we want to retain. The dimensions with a value of 1 indicate the features that are intended to be kept. Furthermore, we directly construct an evaluation sample $\tilde{x} = M \odot x + (1 - M) \odot \mathbf{0}$, which lies outside the distribution that the model is responsible for. Intuitively, this is an appropriate evaluation method that can directly reflect the impact of feature importance.

However, in reality, this process is based on a fundamentally flawed assumption—**that removing a feature means setting it to zero** (the insertion score can be seen as the dual counterpart of the deletion score, which removes unimportant features). In images, zero often represents specific color information, such as black, so **setting values to zero does not equate to removing features**; instead, it may introduce new, semantically meaningful information into the image. For a straightforward example: in a classification task distinguishing **black cats** from **white cats**, the black regions are important features for recognizing the "black cat" class. If we set parts of the image to zero (i.e., turn them black), this does not actually remove the black information—in fact, it may even strengthen the representation of the "black cat." As a result, the model’s confidence output might not decrease and could even increase, which directly contradicts our expectation that the model should fail when important features are removed.

Aside from the issue of introducing additional information, current AEMs also suffer from another obvious heuristic mistake: **it is difficult to ensure that samples with removed features remain valid and realistic samples**. We assume that we have removed 50% of the important features, resulting in images containing half blacked-out regions. However, such samples would never appear in reality. When training the model, we expect it to learn the distribution $P_{x \sim P(x)}(y|x)$, where $P(x)$ represents the true data distribution, and y denotes the class label information. In other words, since the true data distribution occupies only a very small portion of the high-dimensional space, the model only needs to—and can only—be responsible for the distribution of the training data, while a large amount of uncertainty exists outside this distribution. Using model behavior outside the data distribution to evaluate model behavior within the distribution is a highly counterintuitive approach.

In Section 4.3.1 and Section 4.3.2, we analyzed the intermediate images generated by current attribution evaluation methods using OOD detection techniques and image quality evaluation metrics, and found that these samples not only lie outside the true data distribution but also appear highly unrealistic. Since the samples with removed information often lie far from the true distribution $P(x)$, the shift in the model’s output probability distribution during this process may stem not only from biases in the class decision itself but also from discrepancies between the sample and the true distribution $P(x)$. This issue cannot be distinguished during the attribution evaluation process, which undermines the credibility of AEMs. Moreover, because these evaluation results lie in an unstable OOD space, manifesting as very unsmooth insertion and deletion curves, including abnormal phenomena such as confidence increasing when important features are deleted.

Besides Insertion& Deletion Scores, evaluation methods such as Infidelity and Sensitivity- n , although attempting to circumvent the explicit insertion/deletion issues by focusing on consistency or sensitivity, still rely on intervening in the input features during their operations. Consequently, they inevitably introduce intermediate images that deviate from the original distribution, resulting in similar heuristic mistakes in the evaluation outcomes. The issues with the Sensitivity- n metric are similar. Although this metric observes changes in model predictions by randomly occluding a subset of important features selected based on attribution rankings, it fundamentally relies on the assumption that “occlusion is equivalent to feature deletion.”. Meanwhile, these occlusion operations may still introduce unnatural semantic cues or create abnormal structures within the images, thereby affecting the stability of the model’s output. In summary, when designing AEMs, we must rigorously avoid these heuristic mistakes.

3.3 FAITHFULNESS UNDER THE DISTRIBUTION (FUD)

3.3.1 INTUITION

~~Next, let me introduce our FUD evaluation algorithm with a brief summary for clarity. The core idea of FUD is to construct attribution evaluation samples that remain within the distribution while preserving the information to be evaluated. This process involves two key aspects: one is how to ensure the samples stay within the distribution, and the other is how to ensure the preservation of the evaluation information.~~ simple: given an attribution map, we construct

216 perturbed samples that (i) remain on the data manifold and (ii) preserve all visible features that
 217 the attribution method identifies as important, without introducing new evidence that supports the
 218 predicted class y . Conceptually, this corresponds to a diffusion-style inpainting process guided by
 219 a hard mask and by a “no new evidence for class y ” bias, so that the evaluation reflects only the
 220 contribution of the preserved features.

221 For completeness, we note that such perturbations are expected to satisfy several desirable properties,
 222 including in-distribution realism, exact preservation of the retained features, absence of hallucinated
 223 class evidence, and perceptual coherence. These desiderata motivate the FUD update rule, and are
 224 discussed in more detail in Appendix B.

226 3.3.2 DERIVATION

227 We now summarise the FUD evaluation algorithm and formalise the above intuition. The derivation
 228 addresses two questions: how to keep the perturbed samples within the data distribution, and how to
 229 preserve the information we want to evaluate.

231 **Within the distribution** Inspired by the SGM ~~algorithm~~ (Song et al., 2020), we assume that the true
 232 ~~algorithm~~ distribution of samples data is $P(x)$. ~~At the same time, we consider any sample~~ We denote by x^t (It is important
 233 ~~to note that, for consistency of definition, we let $t \in \{1, 2, \dots, T\}$ represent the number of an~~
 234 ~~intermediate sample at iteration $t \in \{1, 2, \dots, T\}$, where t counts the remaining update steps. Each~~
 235 ~~and each update transforms x^t into x^{t-1} , and we set $x^T = M \odot x + (1 - M) \odot \epsilon$, $\epsilon \sim N(0, I)$) lies
 236 ~~outside the data distribution. If we can, we initialise~~~~

$$237 x^T = M \odot x + (1 - M) \odot \epsilon, \quad \epsilon \sim \mathcal{N}(0, I), \quad (1)$$

238 so that the unmasked pixels follow the original image x , while the masked pixels are replaced by
 239 noise; in general, such an x^t lies off the data manifold.

241 If we could obtain the gradient $\nabla_{x^t} P(x^t)$ of the true distribution $\nabla_{x^t} P(x^t)$ at the current posi-
 242 tion at each step, then we can, we could use gradient ascent to update x^t , guiding it to approach
 243 the true distribution. This process can be intuitively illustrated by our demonstration in Figure
 244 1(b), where the small arrows represent the gradient field information. Of course, in practice, since
 245 gradients are very sparse and guide it towards regions of higher density. In practice, gradients in
 246 the input space and the distributional optimization process must satisfy normalization constraints,
 247 we use $\nabla_{x^t} \log P(x^t)$ as an equivalent replacement for the original optimization objective, while
 248 performing gradient descent using $x^{t-1} = x^t + c \cdot \nabla_{x^t} \log P(x^t) + \sqrt{2c} \epsilon$. Here, are very sparse
 249 and the optimisation must satisfy normalisation constraints, so we instead work with the score
 250 function and update according to

$$251 x^{t-1} = x^t + c \nabla_{x^t} \log P(x^t) + \sqrt{2c} \epsilon, \quad \epsilon \sim \mathcal{N}(0, I), \quad (2)$$

252 where c denotes the Langevin step size, and $\epsilon \sim N(0, I)$ represents an additional noise
 253 term (Song et al., 2020). In practical use, we and the noise term follows Song et al. (2020)

254 We approximate the true gradient of the distribution $\nabla_{x^t} \log P(x^t)$ using a score
 255 $\nabla_{x^t} \log P(x^t)$ using a learned score function $s_\theta(x^t)$, meaning that the training objective becomes
 256 $\theta^* = \underset{\theta}{\operatorname{argmin}} \sum_{t=1}^T \lambda(t) \mathbb{E}_{P_{\sigma^t}(x^t)} \left[\|s_\theta(x^t) - \nabla_{x^t} \log P_{\sigma^t}(x^t)\|_2^2 \right]$. Here, $\lambda(t)$ trained with the
 257 standard SGM objective

$$258 \theta^* = \underset{\theta}{\operatorname{argmin}} \sum_{t=1}^T \lambda(t) \mathbb{E}_{P_{\sigma^t}(x^t)} \left[\|s_\theta(x^t) - \nabla_{x^t} \log P_{\sigma^t}(x^t)\|_2^2 \right], \quad (3)$$

259 where $\lambda(t)$ and σ^t are pre-defined hyperparameters. Of course, $s_\theta(x^t)$ can be equivalently learned
 260 from diffusion models using strategies like The score s_θ can also be learned via diffusion models
 261 such as DDPM (Ho et al., 2020). Since this paper does not cover that part of the training, the details
 262 can be found in focus on the training details, we refer the reader to SGM (Song et al., 2020). To

briefly summarize: ~~once we obtain the gradient information of the distribution, we can use it to update samples via gradient steps to bring them back within the distribution.~~; here it is sufficient to note that, once we obtain the gradient information of the distribution, we can update samples using gradient steps to bring them back within the distribution.

Preservation of the evaluation information During the evaluation of attribution methods, we progressively remove or modify varying proportions of features that the attribution method deems unimportant, thereby preserving more the features that are crucial to the model’s decision-making. The goal of FUD is to continue preserving the features that need to be evaluated, while simultaneously ensuring that the new evaluation samples remain FUD aims to generate evaluation samples that both stay within the data distribution. In this process, we must ensure two important conditions: 1) ~~The features that need to be evaluated must be preserved.~~ 2) ~~No features that bring the sample closer to a different class distribution are generated.~~ Because in the evaluation process, we aim to assess the importance of the remaining features for the model’s decision on the class, if the generation process creates new features related to the class and preserve precisely these features. To achieve this, we will be unable to distinguish whether the contribution comes from the preserved features or the newly generated ones. To satisfy this condition, we assume that we have a new distribution $\tilde{P}(y|x^t)$, the gradients of distributions $\tilde{P}(y|x^t)$ and $P(y|x^t)$ point in opposite directions, that is, $\nabla_{x^t} \tilde{P}(y|x^t) = -\nabla_{x^t} P(y|x^t)$. For ease of derivation, we define this event as require that the features to be evaluated are kept intact, and that no newly generated features bring the sample closer to a different class distribution. Otherwise, it becomes impossible to disentangle the effect of the original preserved features from that of newly created, class-supporting evidence.

To enforce this constraint, we introduce a hypothetical distribution $\tilde{P}(y|x^t)$ whose gradient is opposite to that of $P(y|x^t)$,

$$\nabla_{x^t} \tilde{P}(y|x^t) = -\nabla_{x^t} P(y|x^t), \quad (4)$$

and we denote this “no new class evidence” bias as an event z . At this point, the expected The target distribution that FUD aims to learn is: sample from is then

$$\begin{aligned} P(x^t | z, \tilde{x}, M) &= \frac{P(z, \tilde{x} | x^t, M) P(x^t | M)}{P(z, \tilde{x} | M)} \\ &= \frac{P(z | x^t) P(\tilde{x} | x^t, M) P(x^t)}{P(z, \tilde{x} | M)} \propto P(x^t) P(z | x^t) P(\tilde{x} | x^t, M), \end{aligned} \quad (5)$$

Here, $P(z, \tilde{x} | M)$ denotes a constant. If the prior distribution where $P(z, \tilde{x} | M)$ is a normalising constant and $P(x^t | M) = P(x^t)$ if the prior is independent of M , then it follows that $P(x^t | M) = P(x^t)$. At this point, if we compute the gradient in the same manner as before, we obtain: Taking gradients yields

$$\nabla_{x^t} \log P(x^t | z, \tilde{x}, M) = \nabla_{x^t} \log P(x^t) - \nabla_{x^t} \log P(y | x^t) + \nabla_{x^t} \log P(\tilde{x} | x^t, M), \quad (6)$$

with all gradients taken with respect to x^t .

The part related to $\nabla_{x^t} \log P(x^t)$ can be obtained using the $s_\theta(x^t)$ learned earlier in the paper. The $\nabla_{x^t} \log P(y|x^t)$ part can be obtained using the model corresponding to In this expression, the first term $\nabla_{x^t} \log P(x^t)$ is the image prior $P(x)$ (not a label vector) and is provided by the learned score network $s_\theta(x^t)$. The second term $\nabla_{x^t} \log P(y|x^t)$ is the classifier’s input gradient with respect to x^t , supplied by the model whose behaviour we evaluate; in later steps, we only activate this term after x^t has moved sufficiently close to the data manifold. The third term $\nabla_{x^t} \log P(\tilde{x} | x^t, M)$ enforces consistency on the unmasked pixels. Choosing

$$P(\tilde{x} | x^t, M) = \prod_{M_i=1} \delta(x_i^t - \tilde{x}_i) \quad (7)$$

ensures that these coordinates remain fixed, effectively combining the score-model prior, the behavior being evaluated. It is worth noting that the computation of this term must also adhere

to the principle of remaining within the data distribution, and we will discuss the details of this later. Since $\nabla_{x^t} \log P(\tilde{x} | x^t, M)$ needs to fully preserve the features to be evaluated, we use $P(\tilde{x} | x^t, M) = \prod_{M_i=1} \delta(x_i^t - \tilde{x}_i)$ to represent it. Here, $\delta(\cdot)$ denotes the Dirac distribution. Thus, when $M_i = 1$, the gradient must be infinitely large to ensure consistency with \tilde{x} . Detailed properties are provided in the Appendix C. In practice, classifier-gradient correction, and the hard masking constraint into a single update rule in Eq. (2). In implementation, we directly replace the corresponding part entries of x^t with \tilde{x} whenever $M_i = 1$; further properties are provided in Appendix C.

Now, looking back at the construction of $\nabla_{x^t} \log P(y | x^t)$, this expression The construction of $\nabla_{x^t} \log P(y | x^t)$ can be seen as taking the gradient of the input sample with respect to the negative cross-entropy loss function. However, as we mentioned earlier, the model’s behavior is only reliable for samples within the distribution. In this process, we need to ensure that x^t remains within the distribution. Obviously, the initially updated the model behaviour is reliable only for samples that lie within the data distribution. The initial sample x^T will lie outside the distribution is far from the manifold, and the initially obtained $\nabla_{x^t} \log P(y | x^t)$ also lacks reference significance (The gradient information of a similar nature in SGM requires additional training of the model, sacrificing classification performance to enable it to provide effective gradient information corresponding $\nabla_{x^t} \log P(y | x^t)$ is therefore not meaningful. In SGM-like approaches, similar gradients require additional training that sacrifices classification performance in order to obtain useful gradients on noisy samples. This approach does not allow for the evaluation of extra models). Therefore, in this process, which is incompatible with evaluating arbitrary pretrained models. To avoid this, we initially use $P(x^t | \tilde{x}, M) = \frac{P(\tilde{x} | x^t, M) \cdot P(x^t)}{P(\tilde{x} | M)} \propto P(x^t) \cdot P(\tilde{x} | x^t, M)$ to replace the distribution ignore the z -term and use

$$P(x^t | \tilde{x}, M) = \frac{P(\tilde{x} | x^t, M) P(x^t)}{P(\tilde{x} | M)} \propto P(x^t) P(\tilde{x} | x^t, M) \quad (8)$$

instead of $P(x^t | z, \tilde{x}, M)$, so that the samples move using only the score prior and mask constraint to move samples closer to the distribution. In the manifold. In Appendix D, we use show empirically, using the score function to generate evaluation samples and find that when updating $P(x^t | \tilde{x}, M)$ for about 5%, that after updating $P(x^t | \tilde{x}, M)$ for about 5% of the remaining sampling steps, the samples begin to enter the space within the distribution. At the same time, since features close to the original class sample distribution cannot be generated, we replace the distribution with the originally designed $P(x^t | z, \tilde{x}, M)$ at this point, and then proceed to generate in-distribution region. At that point, features close to the original class distribution have not yet been newly generated, so we switch to the original target distribution $P(x^t | z, \tilde{x}, M)$ and continue sampling to obtain high-quality evaluation samples.

Finally, we need to add some implementation details regarding the use of FUD. FUD can generate attribution summarise how FUD is used as an evaluation metric. FUD generates attribution-evaluation samples that remain stay within the distribution while preserving the information that needs features that need to be evaluated. Therefore, we can follow the design of the deletion score by continuously removing unimportant features \cdot , and during this removal process, use the FUD method with consistent parameters. We follow a deletion-style protocol: we progressively remove features deemed unimportant by the attribution method, use FUD (with fixed hyperparameters) to generate the corresponding evaluation samples \cdot , then observe the changes in the model’s confidence at each removal level, and track the model’s confidence on these samples. If the attribution algorithm can accurately assess important features, it means that evaluation samples retaining the same proportion of features will exhibit higher confidence. The reason why we only focus on retaining If an attribution algorithm can accurately identify important features, rather than designing two separate removal modes like insertion score and deletion score, is that then evaluation samples retaining the same proportion of features will exhibit higher confidence. We only consider this “retain-important-features” direction, rather than defining separate insertion and deletion scores, because evaluating samples where only unimportant features are retained is very likely to be meaningless. For example, if we want to perform the black cat and white cat classification mentioned above, where the cat’s background is grass, retaining two kept is often not informative (for example, keeping a few background patches of grass and debating which of these features

Table 1: Mainstream attribution evaluation metrics compared with FUD.

Metric	Description
Insertion & Deletion (INS/DEL)	Measures change in model output after iteratively inserting / deleting high-score regions.
Infidelity (INFID)	Expected squared error between attribution-weighted perturbations and output change.
Sensitivity- N (Sen- N)	Correlation between output change and random masking of the top- N salient features.

is more important for identifying the cat is unnecessary. Meanwhile, from the perspective of metric implementation, due to in a black-cat vs. white-cat task). From an optimisation perspective, the presence of $-\nabla_{x^t} \log P(y | x^t)$, evaluating the "unimportant" features runs counter to the optimization objective. Adversarial effects can cause instability in the evaluation the $-\nabla_{x^t} \log P(y | x^t)$ term also means that explicitly evaluating "unimportant" features would tend to amplify adversarial effects and destabilise the metric, making it impossible to distinguish whether a feature is truly unimportant or if it is due to excessive influence from $-\nabla_{x^t} \log P(y | x^t)$ difficult to distinguish truly unimportant features from artefacts introduced by this term. The pseudocode of our FUD algorithm can be found in the is provided in Appendix E.

4 EXPERIMENT

4.1 EXPERIMENTAL SETUP

Models & Data. To demonstrate that the proposed evaluation scheme generalises across network families, we test one convolutional and one transformer backbone: RESNET-50 (He et al., 2016)—the canonical ImageNet convolutional network—and VIT-B/16 (Dosovitskiy, 2020), a vision transformer of comparable capacity. Both checkpoints are the publicly released ImageNet-1k weights and are kept *frozen* during every attribution run, thereby eliminating confounding factors that fine-tuning could introduce. Following Pan et al. (2021) and Long et al. (2022), we draw 1,000 validation images uniformly at random from ImageNet (Deng et al., 2009). No further curation is performed, so the subset retains the long-tailed distribution of object categories and recording conditions; each attribution method is therefore evaluated on exactly the same, unbiased sample.

Attribution Baselines. We benchmark eleven representative explainability techniques that collectively cover gradient-, perturbation-, and attack-based families: FIG (Hesse et al., 2021), GIG (Kapishnikov et al., 2021), IG (Sundararajan et al., 2017), BIG (Wang et al., 2021), SM (Simonyan et al., 2013), MFABA (Zhu et al., 2024c), ATTEXPLORE (Zhu et al., 2024b), ISA (Zhu et al., 2024a), EG (Erion et al., 2021), AGI (Pan et al., 2021), and LA (Zhu et al., 2024d). All algorithms are executed with the hyper-parameters recommended by their authors.

Competing Evaluation Criteria. To test whether the **proposed metric (FUD)** in Section 3 yields a more faithful signal of explanation quality, we compare it against three widely used quantitative criteria, summarised in Table 1.

Implementation Details. All experiments run on two NVIDIA L40S GPUs (48 GB) with PyTorch 2.4.1. Mixed-precision inference (FP16) is enabled wherever supported, yielding a $\sim 1.7\times$ speed-up without compromising numerical stability. Following standard practice in generative-model evaluation, we adopt deterministic image-quality metrics (PSNR, SSIM, MS-SSIM, FSIM, GMSD, HaarPSI, VSI) that return fixed scores for each image pair, computed via the PyTorch Image Quality library with default configurations. We set the random seed to 3407 for reproducibility, following Picard (2021). Results are reported as averages over all test samples, consistent with diffusion-model evaluation protocols (Ho et al., 2020).

FUD Diffusion Configuration. FUD employs an unconditional diffusion generator `256x256_diffusion_uncond.pt`. The underlying U-Net has 256 base channels, two residual blocks per resolution, and multi-head self-attention at 32, 16, and 8 pixels (head dim. 64). All residual blocks include up/down sampling with scale-shift normalisation. We adopt FP16 arithmetic and a 1 000-step linear noise schedule while learning both mean and variance (`learn_sigma=True`). Although the generator is class-agnostic, we steer the reverse process with a pretrained classifier (`256x256_classifier.pt`); a guidance scale of 4.0 plus classifier-free guidance weight 2.0

432 balances diversity and fidelity. Each of the 1 000 ImageNet images is explained at 256×256 resolution
 433 with batch size 2.

435 4.2 COMPUTATIONAL CONSIDERATIONS

437 While FUD provides more reliable attribution evaluations by ensuring in-distribution samples, it
 438 introduces additional computational overhead compared to standard deletion/insertion methods.
 439 Generating diffusion-based samples for each masking step requires approximately a few seconds per
 440 image on modern GPUs, whereas traditional zero-masking is virtually instantaneous. This trade-off
 441 between evaluation fidelity and computational efficiency is inherent to our approach. In practice, the
 442 generative model needs to be trained only once per dataset and can be reused across all evaluations,
 443 amortizing the initial cost. We view this overhead as a worthwhile investment for obtaining more
 444 faithful attribution assessments. [Appendix I.3 \(Table 10\) reports wall-clock times on ViT-B/16 for
 445 different numbers of diffusion steps.](#)

447 4.3 EXPERIMENTAL RESULTS

448 We conduct extensive experiments to validate the proposed FUD evaluation scheme against existing
 449 attribution evaluation metrics. Unless otherwise specified, all reported results are averaged over 198
 450 runs for fairness (complete raw results are available in the supplementary repository). We compare
 451 FUD with three widely-used evaluation methods – Insertion/Deletion (INS/DEL), Sensitivity-N
 452 (Sen-N), and Infidelity (INFID) – using two representative models (RESNET-50 and ViT-B/16)
 453 and eleven attribution methods spanning gradient- and perturbation-based explainer families. In the
 454 following, we analyze the authenticity of intermediate samples and the stability of the evaluation
 455 process, and we examine an ablation on our hard vs. soft mask constraints.

457 4.3.1 COMPARISON WITH EXISTING EVALUATION METRICS

458 Our first experiment demonstrates that conventional evaluation metrics produce intermediate samples
 459 that significantly deviate from the training distribution, whereas FUD generates intermediate samples
 460 that remain largely *in-distribution*. We verify this claim by employing Energy (Liu et al., 2020)
 461 as our out-of-distribution (OOD) detector to distinguish intermediate samples from genuine in-
 462 distribution (ID) data. The results in Table 2 show that intermediate inputs produced by INS/DEL,
 463 Sen-N, and INFID are easily recognized as OOD, while those produced by FUD are much harder
 464 to distinguish from normal inputs. For instance, under RESNET-50, the OOD detector achieves a
 465 high AUROC of 0.8974 on INS/DEL samples, but only 0.6863 on FUD’s samples (closer to 0.5,
 466 which indicates random guessing). [3 For completeness, additional perceptual and structural fidelity
 467 comparisons are provided in Table 9 \(Appendix I.1\), showing that FUD yields substantially higher
 468 PSNR/SSIM/FSIM scores than existing metrics.](#)

469 Similarly, the detector’s false positive rate at 95%
 470 TPR (FPR_{95}) jumps from 0.36 (INS/DEL) to 0.83 for
 471 FUD, and FUD yields markedly lower AUPR-In/Out
 472 values than others. In other words, FUD’s transitional
 473 examples are so realistic that the detector struggles to
 474 tell them apart from ID data, whereas other methods
 475 produce “artificial” inputs with obvious OOD char-
 476 acteristics that are readily identified. The reason is
 477 that traditional metrics rely on naive feature removal
 478 or perturbation (e.g. replacing content with zeros or
 479 blurred backgrounds), which introduces semantic bi-
 480 ases (such as large black or noisy regions) not seen
 481 in the training distribution. This distribution shift can
 482 spuriously alter the model’s behavior, undermining
 483 the fidelity evaluation. By contrast, FUD leverages a
 484 learned score function to gradually nudge perturbed
 485 inputs back towards the data manifold while preserv-
 ing the important features, thereby yielding much
 more authentic intermediate samples. As a qualita-

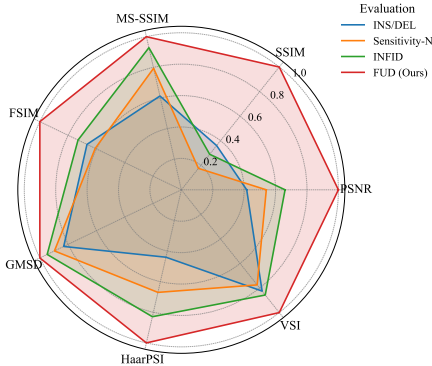


Figure 2: Radar plot of normalised image-quality metrics (GMSD inverted). FUD encloses the largest area, indicating the highest overall fidelity.

Table 2: OOD detection performance for intermediate evaluation samples (higher values indicate easier detection as OOD). We report AUROC (higher means better OOD discrimination), FPR₉₅ (false positive rate at 95% true positive rate), AUPR-In, and AUPR-Out for a standard OOD detector distinguishing intermediate samples (OOD) from normal validation images (ID). **Bold** highlights the values indicating the **most ID-like (hardest to detect)** samples in each case. *Note:* In this context, AUROC, AUPR-In, and AUPR-Out values approaching 0.5 indicate maximal uncertainty in distinguishing between ID and OOD samples, thus reflecting increased in-distribution similarity and greater detection difficulty.

Evaluation	RESNET-50				ViT-B/16			
	AUROC ↓	FPR ₉₅ ↑	AUPR-In ↓	AUPR-Out ↓	AUROC ↓	FPR ₉₅ ↑	AUPR-In ↓	AUPR-Out ↓
INS/DEL	0.8974	0.3603	0.8948	0.8893	0.8784	0.4761	0.8529	0.8894
Sen-N	0.8773	0.5450	0.8579	0.8864	0.8781	0.5660	0.8568	0.8734
INFID	0.7801	0.7720	0.7526	0.7876	0.8181	0.7390	0.7904	0.8119
FUD (Ours)	0.6863	0.8317	0.6660	0.6922	0.6450	0.9404	0.5827	0.6812

Table 3: Average image-quality scores of transitional samples produced by four evaluation metrics. Best values are **bold**.

Evaluation	PSNR ↑	SSIM ↑	MS-SSIM ↑	FSIM ↑	GMSD ↓	HaarPSI ↑	VSI ↑
INS/DEL	10.49	0.27	0.48	0.58	0.271	0.292	0.780
Sensitivity-N	13.63	0.13	0.62	0.53	0.214	0.444	0.732
INFID	16.64	0.22	0.72	0.63	0.169	0.550	0.810
FUD (Ours)	25.20	0.75	0.78	0.86	0.124	0.663	0.946

tive illustration, we provide examples of the progressive masking process under INS/DEL versus FUD in the [appendix F—under FUD](#), [Appendix F](#); as noted in prior work (Jacovi & Goldberg, 2020) [faithful explanations should be grounded in the model’s representation space rather than human visual preferences, so even when extreme deletion ratios make some FUD samples appear less visually intuitive, they nevertheless remain on the model’s in-distribution manifold. Under FUD, the model’s confidence decays much more smoothly without abrupt jumps.](#) Additional comparisons with recent OOD-aware attribution evaluation protocols are reported in Appendix I, further confirming FUD’s advantage in maintaining in-distribution intermediate samples. [A detailed analysis of the \$L_2\$ distance between the perturbed images and the original inputs is provided in Appendix J.](#)

4.3.2 AUTHENTICITY OF TRANSITIONAL SAMPLES

While the OOD detector in Section 4.3.1 confirms *distributional* realism, we further quantify the *perceptual* and *structural* fidelity of transitional images with seven standard quality metrics; a concise summary is given in Table 6, and detailed definitions can be found in Appendix F.

Protocol. Eleven attribution methods are evaluated on RESNET-50 and ViT-B/16. Following standard practice, we progressively mask the top-ranked pixels from 10% to 90% (step 10%), yielding $11 \times 2 \times 9 = 198$ runs per metric. We average each metric across all runs, obtaining Table 3, and visualise the normalised values in Figure 2.

Discussion. Across *all seven* metrics FUD outperforms prior evaluations by a substantial margin. Its PSNR is +8.6 dB higher than the next best (INFID), SSIM improves by ~ 0.53 , and the distortion-oriented GMSD drops by $> 25\%$. Qualitatively, FUD’s intermediate images preserve fine texture and colour consistency, whereas INS/DEL and Sensitivity-N introduce large black or noisy regions, and INFID yields blur artefacts. Combined with the OOD analysis, these results show that FUD produces transitional samples that are not only statistically in-distribution but also perceptually faithful, providing a solid foundation for reliable attribution evaluation.

4.3.3 SMOOTHNESS OF THE EVALUATION PROCESS

We quantitatively assess the *stability* and *monotonicity* of attribution evaluation under different metrics. Ideally, as more important features are removed, the model’s confidence should decrease smoothly

Table 4: Smoothness of the evaluation process, measured by Kendall’s τ (higher values indicate a more monotonic, smoother confidence decrease during feature removal). We compare eleven attribution methods evaluated under INS/DEL vs. under FUD. **Bold** numbers indicate the higher (smoother) value for each attribution method.

Model	Eval.	AGI	LA	AttExp	BIG	EG	FIG	GIG	IG	ISA	MFABA	SM
RESNET-50	INS/DEL	0.6496	0.5771	0.7944	0.6379	0.5730	0.2006	0.2128	0.2176	0.6983	0.6774	0.2833
	FUD (Ours)	0.8443	0.8515	0.8771	0.9129	0.8292	0.8529	0.6845	0.6905	0.8312	0.9259	0.6728
ViT-B/16	INS/DEL	0.7374	0.5501	0.7407	0.7354	0.6495	0.3767	0.4523	0.4615	0.6629	0.7406	0.6015
	FUD (Ours)	0.9174	0.9060	0.9241	0.9046	0.8203	0.8654	0.7741	0.7803	0.8763	0.9206	0.7472

Table 5: Comparison of generated image fidelity under **hard** vs. **soft** mask constraints in FUD (using IG at 50% masking). Higher values indicate better quality for PSNR, SSIM, MS-SSIM, FSIM, HaarPSI, VSI, while lower is better for the distortion metric GMSD. **Bold** denotes the better result for each metric.

Constraint	PSNR \uparrow	SSIM \uparrow	MS-SSIM \uparrow	FSIM \uparrow	GMSD \downarrow	HaarPSI \uparrow	VSI \uparrow
Hard (Ours)	34.0335	0.947984	0.985258	0.970190	0.035163	0.921655	0.991347
Soft	27.6317	0.830200	0.951012	0.916191	0.081117	0.794670	0.971782

and monotonically; irregular rises or plateaus indicate unreliability. We measure smoothness with Kendall’s τ , which captures a sequence’s monotonic trend via pairwise-order concordance. A value of $\tau = 1$ denotes perfectly monotonic decreasing confidence (each removal step strictly reduces the score), whereas values near 0 indicate no clear trend (many out-of-order fluctuations). Table 4 reports τ for deletion sequences from eleven attribution methods evaluated with INS/DEL versus with FUD. FUD makes the process substantially more orderly and smooth: on RESNET-50, FUD gives $\tau > 0.8$ for most explainers, while INS/DEL often yields $\tau < 0.6$ (and as low as 0.21 for gradient-based methods). Notably, IG and GIG, which score very low under INS/DEL ($\tau \approx 0.22$), reach much higher monotonicity with FUD ($\tau \approx 0.69$). A similar trend appears on ViT-B/16; e.g., IG improves from 0.46 to 0.78 under FUD. The higher τ values indicate that confidence decreases more consistently as important features are removed, without the erratic jumps or counter-intuitive increases seen with traditional masking. This monotonic behavior suggests that FUD’s in-distribution samples provide more stable, interpretable signals for attribution evaluation and produce a smoother confidence decay. [We also report additional OOD-detection results for intermediate samples in Table 11 \(Appendix I.2\), which further confirm that FUD produces ID-like transitions that support smoother and more stable confidence decay.](#) By keeping intermediate samples realistic, FUD ensures that each incremental removal yields a proportional, stable change in output, aligning with the ideal of a faithful attribution metric. [A more detailed discussion of what FUD measures, together with a quantitative comparison of FUD scores across 11 representative attribution methods, is provided in Appendix G \(Table 7\).](#)

4.3.4 EFFECT OF SOFT VS. HARD CONSTRAINTS ON IMAGE QUALITY

We ablate *soft* versus *hard* mask constraints in FUD. By default (hard), masked features are fixed to a baseline, i.e., a binary gate that fully removes selected features. As a soft alternative, inspired by Song et al. (2020) and related work, we fill masked regions with Gaussian noise centered at the original values. Formally, instead of $\prod_{i=1}^m \delta(x_i^t - \tilde{x}_i)$ to enforce $\tilde{x}_i = x_i^t$ for unmasked features, we sample $\tilde{x} \sim \mathcal{N}(M \odot x^t, \sigma^2 I)$ where M is a binary mask (1=preserve, 0=remove), yielding the score $\nabla_{x^t} \log P(\tilde{x} | x^t, M) = \frac{M \odot (\tilde{x} - x^t)}{\sigma^2}$. This soft constraint adds noise in preserved regions, potentially smoothing transitions. However, it significantly *degrades* image fidelity. Pixel-level masks often induce incoherent noise, lowering quality. We evaluate fidelity under both settings by applying Integrated Gradients (IG) on 50% masked inputs and computing standard image-quality metrics. Table 5 shows that hard masking yields higher PSNR/SSIM/MS-SSIM/FSIM and lower GMSD; specifically, PSNR/SSIM of **34.03/0.948** vs. 27.63/0.830 for soft. These results confirm that the hard constraint produces more realistic, coherent transitional images, which is critical for reliable evaluation. Therefore, we adopt the hard constraint in FUD by default to maintain high image fidelity and stable performance.

5 CONCLUSION AND FUTURE WORK

FUD evaluates attribution maps in a distribution-aware way by reconstructing masked regions via a score-based diffusion process, keeping transitional samples on the data manifold. This yields more realistic, perceptually faithful, and smoother evaluation dynamics than heuristic baselines. Given compute limits (and to avoid perfectionism), we leave several optimizations for future work: (i) task-specific score functions $s_\theta(x^t)$ tailored to attribution evaluation—the current $s_\theta(x^t)$ is an unconditional guided-diffusion model trained on ImageNet and requires resolution alignment¹; and (ii) more efficient samplers (e.g., DPM-Solver, DDIM) to mitigate the sample-generation bottleneck. At extreme deletion ratios, fills may look unnatural to humans due to limited context yet remain *model-in-distribution* under objective detectors; our evaluation adheres to this model-centric criterion. Future improvements in estimating the data-distribution score $\nabla_x \log P(x)$ may further reduce these limitations, as our framework can seamlessly incorporate stronger generative priors.

ETHICS STATEMENT

We have read and will adhere to the ICLR Code of Ethics. This work uses only public data, involves no human subjects or personally identifiable information, and therefore does not require IRB review. Results are reported for research purposes only; we release anonymized code/configurations to support verification, and will disclose any funding sources and potential conflicts of interest upon acceptance.

REPRODUCIBILITY STATEMENT

To support reproducibility, we release an anonymized repository with all experiment details including training/evaluation scripts, default hyperparameters, configuration files, and software/hardware environment.

REFERENCES

- Chirag Agarwal and Anh Nguyen. Explaining image classifiers by removing input features using generative models. In *Proceedings of the Asian Conference on Computer Vision*, 2020.
- Marco Ancona, Enea Ceolini, Cengiz Öztireli, and Markus Gross. Towards better understanding of gradient-based attribution methods for deep neural networks. *arXiv preprint arXiv:1711.06104*, 2017.
- Mihalj Bakator and Dragica Radosav. Deep learning and medical diagnosis: A review of literature. *Multimodal Technologies and Interaction*, 2(3):47, 2018.
- Chun-Hao Chang, Elliot Creager, Anna Goldenberg, and David Duvenaud. Explaining image classifiers by counterfactual generation. In *International Conference on Learning Representations*, 2019.
- Jia Deng, Wei Dong, Richard Socher, Li-Jia Li, Kai Li, and Li Fei-Fei. Imagenet: A large-scale hierarchical image database. In *2009 IEEE conference on computer vision and pattern recognition*, pp. 248–255. Ieee, 2009.
- Alexey Dosovitskiy. An image is worth 16x16 words: Transformers for image recognition at scale. *arXiv preprint arXiv:2010.11929*, 2020.
- Gabriel Erion, Joseph D Janizek, Pascal Sturmfels, Scott M Lundberg, and Su-In Lee. Improving performance of deep learning models with axiomatic attribution priors and expected gradients. *Nature machine intelligence*, 3(7):620–631, 2021.
- Ruth Fong, Mandela Patrick, and Andrea Vedaldi. Understanding deep networks via extremal perturbations and smooth masks. In *Proceedings of the IEEE/CVF international conference on computer vision*, pp. 2950–2958, 2019.

¹<https://github.com/openai/guided-diffusion>

- 648 Ruth C Fong and Andrea Vedaldi. Interpretable explanations of black boxes by meaningful perturba-
649 tion. In *Proceedings of the IEEE international conference on computer vision*, pp. 3429–3437,
650 2017.
- 651 Arne Gevaert, Axel-Jan Rousseau, Thijs Becker, Dirk Valkenburg, Tijl De Bie, and Yvan Saeys.
652 Evaluating feature attribution methods in the image domain. *Machine Learning*, 113(9):6019–6064,
653 2024.
- 654 Sorin Grigorescu, Bogdan Trasnea, Tiberiu Cocias, and Gigel Macesanu. A survey of deep learning
655 techniques for autonomous driving. *Journal of field robotics*, 37(3):362–386, 2020.
- 656 Kaiming He, Xiangyu Zhang, Shaoqing Ren, and Jian Sun. Deep residual learning for image
657 recognition. In *Proceedings of the IEEE conference on computer vision and pattern recognition*,
658 pp. 770–778, 2016.
- 659 Robin Hesse, Simone Schaub-Meyer, and Stefan Roth. Fast axiomatic attribution for neural networks.
660 *Advances in Neural Information Processing Systems*, 34:19513–19524, 2021.
- 661 Robin Hesse, Simone Schaub-Meyer, and Stefan Roth. Benchmarking the attribution quality of vision
662 models. *Advances in Neural Information Processing Systems*, 37:97928–97947, 2024.
- 663 Jonathan Ho, Ajay Jain, and Pieter Abbeel. Denoising diffusion probabilistic models. *Advances in
664 neural information processing systems*, 33:6840–6851, 2020.
- 665 Alon Jacovi and Yoav Goldberg. Towards faithfully interpretable nlp systems: How should we define
666 and evaluate faithfulness? In *Proceedings of the 58th Annual Meeting of the Association for
667 Computational Linguistics*, pp. 4198–4205, 2020.
- 668 Andrei Kapishnikov, Subhashini Venugopalan, Besim Avci, Ben Wedin, Michael Terry, and Tolga
669 Bolukbasi. Guided integrated gradients: An adaptive path method for removing noise. In
670 *Proceedings of the IEEE/CVF conference on computer vision and pattern recognition*, pp. 5050–
671 5058, 2021.
- 672 Weitang Liu, Xiaoyun Wang, John Owens, and Yixuan Li. Energy-based out-of-distribution detection.
673 *Advances in neural information processing systems*, 33:21464–21475, 2020.
- 674 Yuyang Long, Qilong Zhang, Boheng Zeng, Lianli Gao, Xianglong Liu, Jian Zhang, and Jingkuan
675 Song. Frequency domain model augmentation for adversarial attack. In *European conference on
676 computer vision*, pp. 549–566. Springer, 2022.
- 677 Akib Mashrur, Wei Luo, Nayyar A Zaidi, and Antonio Robles-Kelly. Machine learning for financial
678 risk management: a survey. *Ieee Access*, 8:203203–203223, 2020.
- 679 Lars Nieradzik, Henrike Stephani, and Janis Keuper. Reliable evaluation of attribution maps in cnns:
680 A perturbation-based approach. *International Journal of Computer Vision*, pp. 1–18, 2024.
- 681 Deng Pan, Xin Li, and Dongxiao Zhu. Explaining deep neural network models with adversarial
682 gradient integration. In *Thirtieth International Joint Conference on Artificial Intelligence (IJCAI)*,
683 2021.
- 684 Jeng-Shyang Pan, Gui-Ling Wang, Shu-Chuan Chu, Dongqiang Yang, and Václav Snášel. New
685 feature attribution method for explainable aspect-based sentiment classification. *Knowledge-Based
686 Systems*, 304:112550, 2024.
- 687 Vitali Petsiuk, Abir Das, and Kate Saenko. Rise: Randomized input sampling for explanation of
688 black-box models. *arXiv preprint arXiv:1806.07421*, 2018.
- 689 David Picard. Torch. manual_seed (3407) is all you need: On the influence of random seeds in deep
690 learning architectures for computer vision. *CoRR*, 2021.
- 691 Sukrut Rao, Moritz Böhle, and Bernt Schiele. Towards better understanding attribution methods. In
692 *Proceedings of the IEEE/CVF conference on computer vision and pattern recognition*, pp. 10223–
693 10232, 2022.

- 702 Yao Rong, Tobias Leemann, Vadim Borisov, Gjergji Kasneci, and Enkelejda Kasneci. A consistent
703 and efficient evaluation strategy for attribution methods. In *International Conference on Machine*
704 *Learning*, pp. 18770–18795. PMLR, 2022.
- 705
706 Karen Simonyan, Andrea Vedaldi, and Andrew Zisserman. Deep inside convolutional networks:
707 Visualising image classification models and saliency maps. *arXiv preprint arXiv:1312.6034*, 2013.
- 708 Yang Song, Jascha Sohl-Dickstein, Diederik P Kingma, Abhishek Kumar, Stefano Ermon, and Ben
709 Poole. Score-based generative modeling through stochastic differential equations. *arXiv preprint*
710 *arXiv:2011.13456*, 2020.
- 711
712 Pascal Sturmfels, Scott Lundberg, and Su-In Lee. Visualizing the impact of feature attribution
713 baselines. *Distill*, 5(1):e22, 2020.
- 714 Mukund Sundararajan, Ankur Taly, and Qiqi Yan. Axiomatic attribution for deep networks. In
715 *International conference on machine learning*, pp. 3319–3328. PMLR, 2017.
- 716
717 Bas HM Van der Velden, Hugo J Kuijf, Kenneth GA Gilhuijs, and Max A Viergever. Explainable
718 artificial intelligence (xai) in deep learning-based medical image analysis. *Medical Image Analysis*,
719 79:102470, 2022.
- 720 Zifan Wang, Matt Fredrikson, and Anupam Datta. Robust models are more interpretable because
721 attributions look normal. *arXiv preprint arXiv:2103.11257*, 2021.
- 722
723 Chih-Kuan Yeh, Cheng-Yu Hsieh, Arun Suggala, David I Inouye, and Pradeep K Ravikumar. On the
724 (in) fidelity and sensitivity of explanations. *Advances in neural information processing systems*,
725 32, 2019.
- 726 Tianxi Yu, Xiaoyao Yin, Menglin Yao, and Tong Liu. Network security monitoring method based on
727 deep learning. In *Journal of Physics: Conference Series*, volume 1955, pp. 012040. IOP Publishing,
728 2021.
- 729
730 Zhiyu Zhu, Huaming Chen, Xinyi Wang, Jiayu Zhang, Zhibo Jin, Jason Xue, and Jun Shen. Iterative
731 search attribution for deep neural networks. In *Forty-first International Conference on Machine*
732 *Learning*, 2024a.
- 733
734 Zhiyu Zhu, Huaming Chen, Jiayu Zhang, Xinyi Wang, Zhibo Jin, Jason Xue, and Flora D Salim.
735 Attexplore: Attribution for explanation with model parameters exploration. In *The Twelfth*
International Conference on Learning Representations, 2024b.
- 736
737 Zhiyu Zhu, Huaming Chen, Jiayu Zhang, Xinyi Wang, Zhibo Jin, Minhui Xue, Dongxiao Zhu, and
738 Kim-Kwang Raymond Choo. Mfaba: a more faithful and accelerated boundary-based attribution
739 method for deep neural networks. In *Proceedings of the AAAI Conference on Artificial Intelligence*,
740 volume 38, pp. 17228–17236, 2024c.
- 741
742 Zhiyu Zhu, Zhibo Jin, Jiayu Zhang, and Huaming Chen. Enhancing model interpretability with local
743 attribution over global exploration. In *Proceedings of the 32nd ACM International Conference on*
Multimedia, pp. 5347–5355, 2024d.
- 744
745
746
747
748
749
750
751
752
753
754
755

LLM USAGE DISCLOSURE

We used large language models (OpenAI GPT-4o and GTP-5) as auxiliary tools for grammar checking and language polishing of the manuscript. These models were not involved in research ideation, experimental design, implementation, or analysis. The authors take full responsibility for all content.

A RELATED WORK

A.1 STATE-OF-THE-ART ATTRIBUTION METHODS

Attribution methods have emerged as one of the mainstream approaches for interpreting Deep Neural Networks (DNNs), owing to their ability to provide fine-grained, pixel-level explanations. We begin by introducing several commonly used attribution methods developed in recent years. The Integrated Gradients (IG) method (Sundararajan et al., 2017) addresses the issue of vanishing gradients in Saliency Map (SM) (Simonyan et al., 2013) algorithm by proposing two axioms that attribution should satisfy. IG computes attribution scores for each input feature by integrating the gradients along a straight-line path from a chosen baseline to the input. To mitigate the noise interference along the integration path, the Guided Integrated Gradients (GIG) method (Kapishnikov et al., 2021) introduces constraints on the network input and backpropagates neuron gradients to suppress irrelevant pixel attributions, retaining only those features pertinent to the predicted class. While GIG effectively reduces noise, it is primarily tailored to image-based tasks, is highly sensitive to the quality of input features, and suffers from significant computational complexity. To further improve the rationality of anchor point selection, the Boundary-based Integrated Gradients (BIG) method (Wang et al., 2021) introduces a boundary-search mechanism to achieve more accurate attribution results. BIG attempts to use adversarial examples as anchors but still relies on linear integration paths. Additionally, BIG requires gradient computations for each feature point individually, which substantially increases computational costs. In contrast, the Adversarial Gradient Integration (AGI) method (Pan et al., 2021) seeks the steepest non-linear ascent path starting from adversarial examples, thus avoiding the need for a predefined baseline as required in IG. However, AGI’s effectiveness heavily depends on the quality of adversarial sample generation, and its robustness remains under debate. In addition, other adversarial attribution methods (Zhu et al., 2024b;a;c) that employ adversarial examples as attribution baselines have also been widely adopted.

A.2 COMMONLY USED ATTRIBUTION EVALUATION METRICS

Current attribution evaluation metrics, such as the Insertion & Deletion Scores (Petsiuk et al., 2018), offer an intuitive curve-based evaluation approach. By progressively adding or removing regions with high attribution scores and observing the corresponding changes in prediction probability, these metrics aim to reflect the faithfulness of the attribution. The Deletion Score progressively occludes the pixels with the highest attribution scores (e.g., by setting them to zero or to the mean value), and plots a curve showing how the model’s prediction probability decreases as the proportion of occluded pixels increases. A smaller Area under the Curve (AUC) indicates a more faithful attribution. In contrast, the Insertion Score begins with a blank or blurred baseline and progressively inserts the most important pixels based on attribution scores, observing the rate at which the model’s prediction probability increases. As the Insertion and Deletion Scores often rely on filling removed regions with constant values (e.g., black or mean pixels), they are highly sensitive to distributional shifts. The resulting perturbed inputs—characterized by large artificial occlusions—can diverge substantially from the original data distribution, potentially introducing instability or bias into the evaluation outcomes. Recent research (Nieradzic et al., 2024) have sought to improve the smoothness of attribution maps by introducing adversarial perturbations or enforcing smoothness regularization during the evaluation phase. Nonetheless, such methods fall short in mitigating the distributional shift induced by masking operations, as the modified inputs often remain at the periphery of the training data distribution.

The Infidelity metric (Yeh et al., 2019) attempts to quantify attribution consistency by computing the expected mean squared error between attribution scores and the corresponding changes in model predictions under input perturbations, theoretically providing a more robust estimate. The metric selects a meaningful perturbation distribution (e.g., adding random noise to pixels or occluding a patch), and computes the expected mean squared error between the change in the model’s output

810 and the inner product of the perturbation with the attribution. A lower Infidelity score indicates
 811 higher attribution faithfulness. It is worth noting that the experiments compute the Infidelity metric
 812 using perturbations such as ‘noise baselines’ and ‘patch removal’. However, commonly used global
 813 patch occlusion methods often result in unrealistic images, which may compromise the reliability
 814 of the metric. Although local random noise perturbations tend to cause smaller deviations from the
 815 original data distribution, this assumption still does not fully guarantee alignment with the training
 816 distribution.

817 Another metric for evaluating attribution faithfulness is Sensitivity- n (Ancona et al., 2017), which
 818 emphasizes the consistency between attribution scores and the model’s output response. The core idea
 819 is that if certain pixels (or features) are identified as important in the attribution map, then randomly
 820 occluding these regions should lead to significant changes in the model’s prediction. Specifically,
 821 Sensitivity- n evaluates whether the change in the model’s output is consistent with the attribution
 822 importance by randomly selecting and occluding the top- n features with the highest attribution scores
 823 and measuring the resulting output variation. Unlike the Insertion & Deletion Scores, Sensitivity- n
 824 does not rely on explicitly constructing a perturbation sequence or response curve, making it more
 825 computationally efficient. Moreover, it mitigates the distributional shift issue caused by unnatural
 826 occluded images. However, this metric remains sensitive to the choice of occlusion strategy—for
 827 instance, the selection of occlusion values (e.g., zero or mean replacement) can significantly influence
 828 the results. Moreover, Sensitivity- n does not directly assess the causal explanatory relationship
 829 between the attribution and the model’s prediction, but rather reflects local perturbation consistency.
 830 As a result, it is limited in its ability to serve as a comprehensive evaluation metric.

831 To mitigate the aforementioned issues, some studies have introduced blurring operations as alternatives
 832 to direct occlusion. For instance, the Meaningful Perturbation (Fong & Vedaldi, 2017) and Extremal
 833 Perturbation (Fong et al., 2019) methods optimize masks to maximize the model’s output within
 834 the preserved regions. These methods produce visually more natural perturbations and reduce
 835 abrupt distributional shifts; however, the inherent blurring still preserves low-frequency features
 836 of the original image, which may lead to semantic distortions in the attribution maps. Moreover,
 837 the generated inputs are rarely encountered in the training set, thus still posing a certain risk of
 838 out-of-distribution (OOD) inputs.

839 Beyond blurring-based perturbations, several works have explored the use of generative
 840 models to reconstruct or in-paint the regions removed during attribution. Chang et al. (2019)
 841 generate counterfactual images by replacing selected features with samples from a conditional
 842 generative model, thereby exposing how classifiers depend on specific structures. Similarly,
 843 Agarwal & Nguyen (2020) propose filling removed pixels using a generative model to maintain
 844 perceptual realism while probing feature importance. While these approaches significantly reduce
 845 the visual artifacts of masking, the generative prior may inadvertently introduce class-supporting
 846 evidence rather than faithfully removing it, complicating deletion-based evaluation. Our FUD
 847 framework inherits the insight that perturbations should remain on the data manifold, but applies
 848 it at the level of the *evaluation metric*: any attribution method can be assessed under a unified
 849 score-based generative prior without modifying the explainer itself. Therefore, the design of attribu-
 850 tion metrics must balance ‘distributional consistency’ and ‘interpretability,’ avoiding conclusions
 851 about attribution quality based solely on any single metric.

852 B DESIRABLE PROPERTIES OF EVALUATION PERTURBATIONS

853 To clarify what constitutes a reasonable modified image for attribution evaluation, we list the ideal
 854 properties that any perturbation x' should satisfy:

855 1. **In-distribution realism.** Perturbed samples should remain on (or close to) the data manifold
 856 rather than becoming OOD artifacts. FUD enforces this via the prior term $\nabla_x \log P(x)$ and validates
 857 it through OOD-detection metrics.

858 2. **Preservation of retained features.** Pixels marked as “kept” must match the original input exactly.
 859 This is implemented through the hard constraint $P(\hat{x} | x, M)$ and stepwise overwriting.

860 3. **No hallucinated class evidence.** Perturbations should not introduce features that artificially
 861 increase confidence in class y . FUD controls this via the corrective term $-\nabla_x \log P(y | x)$.

864 **4. Perceptual coherence.** Intermediate samples should remain structurally consistent (edges, colors,
865 textures). This is quantified using standard perceptual metrics such as PSNR, SSIM, FSIM, and
866 GMSD.

867 These desiderata generalize the assumptions underlying baseline-replacement methods. FUD
868 operationalizes them explicitly through the posterior

$$869 P(x_t | z, \tilde{x}, M) \propto P(x_t) P(z | x_t) P(\tilde{x} | x_t, M), \quad (9)$$

870 whose gradient decomposition in Eq. 6 directly corresponds to properties (1)–(3), while (4) is
871 validated empirically.

872 C PROOF OF THE δ -LIKELIHOOD FOR OBSERVED PIXELS

873 For each pixel index i we denote by $M_i = 1$ that the pixel is *observed* (i.e. must be preserved exactly
874 in every evaluation sample) and by $M_i = 0$ that the pixel is *free* (no constraint). Hence the conditional
875 likelihood factorises as

$$876 P(\tilde{x} | x^t, M) = \prod_{M_i=1} \delta(x_i^t - \tilde{x}_i), \quad (10)$$

877 where the Dirac distribution $\delta(\cdot)$ assigns non-zero density *only* when $x_i^t = \tilde{x}_i$, while the factor
878 1 leaves unobserved pixels unconstrained. The support of x^t is therefore restricted to the *linear*
879 *sub-manifold* $\{x^t \in \mathbb{R}^d : x_i^t = \tilde{x}_i \text{ for all } M_i = 1\}$.

880 **Dirac as the zero-variance limit of a Gaussian** To justify the δ -likelihood formally, consider the
881 single-pixel Gaussian proxy

$$882 \mathcal{N}(x_i^t; \tilde{x}_i, \sigma^2) = \frac{1}{\sqrt{2\pi\sigma}} \exp\left[-\frac{(x_i^t - \tilde{x}_i)^2}{2\sigma^2}\right]. \quad (11)$$

883 Taking the limit $\sigma^2 \rightarrow 0$ yields $\mathcal{N}(x_i^t; \tilde{x}_i, \sigma^2) \xrightarrow{\sigma \rightarrow 0} \delta(x_i^t - \tilde{x}_i)$. Multiplying the Gaussian factors
884 over all i with $M_i = 1$ and letting $\sigma^2 \rightarrow 0$ produces precisely the product of Dirac distributions used
885 above.

886 **Intuition** This formulation can be understood as an extreme case of a “zero-variance Gaussian,”
887 where non-zero probability mass exists *only* when $x_{(i)}^t = \tilde{x}_{(i)}$ for observed pixels. That is, the distri-
888 bution has support strictly limited to the set of values that exactly match the ground truth on known
889 entries. For unobserved pixels where $M_i = 0$, the likelihood imposes no constraints—effectively
890 acting as a multiplicative factor of one. As a result, the support of x^t becomes a linear sub-manifold
891 in which all observed pixels must precisely align with their true values. This induces a hard constraint
892 in the generative process: *any valid sample must match the observed data exactly.*

893 **Log-likelihood and gradient** Because $\delta(\cdot)$ is not a conventional density, its logarithm is undefined;
894 nevertheless the *gradient* of the log-likelihood can be obtained safely via the Gaussian limit. For the
895 vector $x^t \in \mathbb{R}^d$ we have

$$896 \log P(\tilde{x} | x^t, M) = \sum_{M_i=1} \log \delta(x_i^t - \tilde{x}_i), \quad (12)$$

$$897 \nabla_{x^t} \log P = \frac{M \odot (\tilde{x} - x^t)}{\sigma^2} \xrightarrow{\sigma \rightarrow 0} \text{a vector pointing towards infinity} \quad (13)$$

898 where \odot denotes the element-wise product and $M \in \{0, 1\}^d$ is the mask vector. As $\sigma \rightarrow 0$, the
899 magnitude of the gradient diverges while its direction always points from x^t back to the true pixel
900 values \tilde{x} : the optimisation is therefore forced *instantaneously* onto the constraint manifold.

901 **Practical implementation** In practice we do not apply the infinite gradient. Instead, after each
902 diffusion update we simply overwrite the observed pixels:

$$903 x^t \leftarrow M \odot \tilde{x} + (1 - M) \odot x^t, \quad (14)$$

904 which is exactly equivalent to following the δ -likelihood’s gradient in the $\sigma^2 \rightarrow 0$ limit but avoids
905 numerical instabilities.

D ADDITIONAL ANALYSIS OF THE SCORE FUNCTION

Why delay the classifier gradient? As argued in Section 3.3.2, adding the classifier term $-\nabla_{x^t} \log P(y | x^t)$ too early can push off-manifold samples further away; guidance is beneficial only after the diffusion trajectory has moved close to the data manifold under the prior score $s_\theta(x^t)$.

This is because at early steps, the sample x^t is still far from the classifier’s data distribution, making the gradient signal from the classifier unreliable or even misleading. Delaying the classifier guidance ensures that meaningful and stable gradients are provided only when the sample is sufficiently close to the data manifold.

Experimental protocol We fix the total diffusion steps at $T = 1000$ and **always** turn on classifier guidance for the last 5% of those steps ($t < 50$). To study the effect across different deletion levels, we vary the mask ratio $\rho \in \{10\%, 20\%, \dots, 90\%\}$, where ρ denotes the percentage of *unimportant* features removed by the attribution method before FUD starts sampling. For each ρ we generate 500 evaluation samples and measure the AUROC between the retained-feature ratio and the classifier confidence.

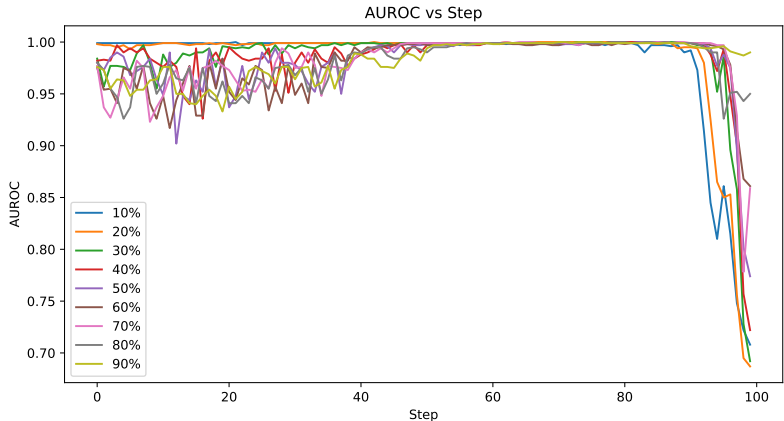


Figure 3: AUROC versus diffusion step for different **mask ratios** ρ (10%–90%). Classifier guidance is enabled for the last 5% of steps (grey vertical line). All curves stabilise quickly after guidance kicks in, and the final AUROC is highest under this 5% schedule.

Results Figure 3 plots AUROC versus diffusion step for six representative mask ratios. A consistent pattern emerges: AUROC remains flat while only the prior $s_\theta(x^t)$ is applied, then climbs sharply once classifier guidance begins at the $t/T = 0.05$ mark, finally saturating within 30–40 steps. Although higher mask ratios (e.g. 70–90 converge to stable curves once guidance is applied, confirming that the “5% switch” is robust across deletion levels.

E PSEUDOCODE FOR FUD EVALUATION

Note: In practice, we use DDIM to accelerate the sampling process. This procedure in Algorithm 1 can be viewed as a discretized version of DDPM sampling.

Algorithm 1: FUD Evaluation

Input: original image \tilde{x} ;
mask M ;
 out-of-distribution *threshold* O ;
 Score Function $S_\theta(x, \varepsilon, t)$;
 classifier $P(y | x)$;
 total steps T , DDIM noise schedule $\{\bar{\alpha}_t\}_{t=0}^T$
Output: in-distribution evaluation sample x^0

$$\varepsilon \sim \mathcal{N}(0, I) \quad x^T \leftarrow \tilde{x} \odot M + \varepsilon \odot (1 - M)$$

for $t = T, \dots, 1$ **do**
 if $t < O$ **then**
 $\hat{\varepsilon} \leftarrow S_\theta(x^t, t)$
 else
 $\hat{\varepsilon} \leftarrow S_\theta(x^t, t) + \sqrt{1 - \bar{\alpha}_t} \nabla_{x^t} \log P(y | x^t)$
 $x^{t-1} \leftarrow \sqrt{\bar{\alpha}_{t-1}} \left(\frac{x^t - \sqrt{1 - \bar{\alpha}_t} \hat{\varepsilon}}{\sqrt{\bar{\alpha}_t}} \right) + \sqrt{1 - \bar{\alpha}_{t-1}} \hat{\varepsilon}$
 $x^{t-1} \leftarrow \tilde{x} \odot M + x^{t-1} \odot (1 - M)$
return x^0

F METRIC DEFINITIONS

Each metric in Table 6 is briefly defined below:

- **PSNR** – Peak Signal-to-Noise Ratio; measures average pixel fidelity.
- **SSIM** – Structural Similarity Index; compares luminance, contrast, and structure.
- **MS-SSIM** – Multi-Scale SSIM; aggregates SSIM over multiple resolutions.
- **FSIM** – Feature Similarity; integrates phase congruency and gradient magnitude.
- **GMSD** – Gradient Magnitude Similarity Deviation; lower values indicate fewer edge distortions.
- **HaarPSI** – Haar Wavelet–based Perceptual Similarity; focuses on multiscale edge recall.
- **VSI** – Visual Saliency–based Index; emphasises fidelity in salient regions.

Table 6: Image–quality metrics used to assess transitional samples. For **GMSD** we invert the score ($1 - \text{GMSD}$) when plotting the radar chart to align “higher-is-better” semantics.

Metric	High Value Means	Low Value Means	Trend
PSNR	Low pixel distortion	Large pixel error	↑
SSIM	High structural similarity	Blurring / structure loss	↑
MS-SSIM	Multi-scale consistency	Local distortion	↑
FSIM	Sharp edges / textures	Edge and detail loss	↑
GMSD	Small gradient deviation	Edge blur, contour loss	↓
HaarPSI	Good multi-scale detail	Global blur	↑
VSI	Clear salient regions	Salient region blur / loss	↑

Comparing FUD to existing deletion baselines. The upper sub-row of each example in Fig. 4 (*Original* → *Heat-map* → *INFD* → *INS/DEL* → *Sen-N*) visualises three widely–used deletion metrics. Despite their popularity, all three baselines exhibit conspicuous off-manifold artefacts even before **half** of the pixels are masked:

- **INFD** (third column) applies a saliency–guided Gaussian blur. At moderate deletion ratios the foreground object dissolves into low-frequency smear, but background textures remain untouched—contradicting the intended focus on “unimportant” regions.

1026
1027
1028
1029
1030
1031
1032
1033
1034
1035
1036
1037
1038
1039
1040
1041
1042
1043
1044
1045
1046
1047
1048
1049
1050
1051
1052
1053
1054
1055
1056
1057
1058
1059
1060
1061
1062
1063
1064
1065
1066
1067
1068
1069
1070
1071
1072
1073
1074
1075
1076
1077
1078
1079

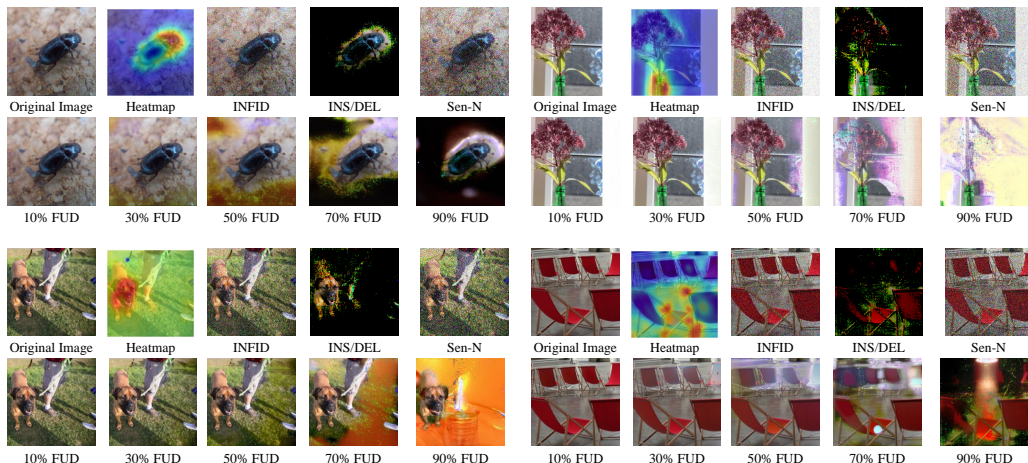


Figure 4: **Qualitative evolution of FUD.** From left to right: original image, LA (Zhu et al., 2024d) heat-map, and FUD samples after deleting $(100 - \rho)\%$ *unimportant* pixels and reconstructing the removed regions via score-based diffusion under the learned data distribution, rather than using any constant black/white filling. The apparent contrast changes therefore come from generative in-painting on the image manifold, not from hard occlusions as in INS/DEL or Sen-N. Rows correspond to four randomly-chosen validation images.

- **INS/DEL** (fourth column) literally *zeros* the unimportant features, producing unnatural black cavities that trigger premature confidence drops and confound any perceptual judgement.
- **Sen-N** (fifth column) injects pixel-wise Gaussian noise; as deletion grows the image devolves into high-frequency snow, masking true object boundaries and violating the data-manifold assumption behind the classifier.

FUD yields natural transitional samples. The lower sub-row shows FUD results for five retained-feature ratios $\rho = 10\%, 30\%, 50\%, 70\%, 90\%$. Three qualitative patterns stand out:

1. **Perceptual realism up to 50 %.** When $\rho \geq 50\%$ the generated evaluation images are almost indistinguishable from the originals in *both* structure and colour palette. Crucially, no “floating” fragments or unnatural voids appear, confirming that FUD keeps the trajectory on the image manifold.
2. **Smooth degradation beyond 50 %.** As the mask ratio increases to 70 – 90 %, FUD removes the object in a coarse-to-fine fashion: salient boundaries blur first, then disappear into context-aware textures. The resulting images are still globally coherent—e.g. the beetle body in Example A melts into surrounding earth tones, and the red deck-chair pattern in Example D fades without breaking symmetry.
3. **No class-switch artefacts.** Even in the extreme 90 % deletion case, FUD never hallucinates features suggestive of a different ImageNet class. This visually supports the theoretical constraint in Eq. (7) that prevents samples from crossing class manifolds.

Implications for metric fidelity. Because FUD maintains high perceptual quality *until* more than half of the high-attribution pixels are removed, the resulting deletion curve (cf. Fig. 6, main paper) reflects *true* model reliance on the preserved features rather than spurious artefacts. Conversely, the rapid confidence collapse observed with INS/DEL or Sen-N can be attributed to their off-manifold distortions rather than to the attribution map itself. Hence FUD provides a more faithful and interpretable evaluation of saliency methods.

G ADDITIONAL ANALYSIS OF WHAT FUD MEASURES

Table 7: FUD, Insertion, Deletion, Sensitivity- n , and INFID scores for 11 representative attribution methods. Higher is better for FUD, Insertion, and Sensitivity- n ; lower is better for Deletion and INFID.

Method	FUD	Insertion	Deletion	Sensitivity- n	INFID
SM	0.282534	0.314616	0.068716	0.141470	0.287042
IG	0.313328	0.344998	0.052537	0.126894	0.129003
FIG	0.208447	0.245956	0.069740	-0.130477	0.277800
BIG	0.354196	0.435646	0.084743	0.027358	0.019717
MFABA	0.276959	0.374439	0.118989	0.034741	0.019622
AttEXplore	0.276253	0.468133	0.056584	0.010449	0.019581
GIG	0.309788	0.332303	0.047974	0.123184	0.113368
AGI	0.318770	0.443992	0.057337	0.013355	0.020138
ISA	0.232271	0.567845	0.101100	0.023021	0.019569
EG	0.274612	0.319021	0.076970	-0.007913	0.219567
LA	0.268251	0.520222	0.054138	0.019070	0.019574

In this section we provide a more detailed discussion of what FUD actually measures and how it affects the ranking of attribution methods.

By design, a higher FUD score indicates that, when we progressively remove the features ranked as “low importance” by an attribution method, the model confidence decreases more slowly and more smoothly along the deletion path. Intuitively: (i) if an attribution method can accurately identify the truly important regions, then removing the features it considers unimportant should keep the model performance relatively high for a longer portion of the deletion trajectory, and the corresponding FUD curve should exhibit a smoother and slower decay; (ii) therefore, a higher FUD score can be interpreted, under the constraint of staying in-distribution, as evidence that the method is more accurate at identifying genuinely important regions.

To make the effect of FUD on the ranking more transparent, we report in Table 7 the scores of 11 representative attribution methods under five evaluation metrics: FUD, Insertion, Deletion, Sensitivity- n , and INFID. Here, higher values are better for FUD, Insertion, and Sensitivity- n , whereas lower values are better for Deletion and INFID. Gradient-path based methods such as BIG, AGI, IG and GIG achieve relatively higher FUD scores, whereas some methods that perform well under conventional Insertion/Deletion metrics (for example, variants that rely on aggressive masking or boundary attacks) move down in the ranking under FUD. Combined with the Kendall’s τ analysis in Sec. 4.3.3, we observe that, under traditional INS/DEL evaluation, methods like IG and GIG can exhibit non-monotonic behaviour and even abnormal confidence increases, while under FUD their deletion curves become much smoother and closer to monotonic decay. This is consistent with the overall pattern in Table 7: FUD not only reorders existing attribution methods, but also clarifies which methods are more trustworthy when evaluated in-distribution and without relying on spurious evidence, thereby changing our empirical judgement about which family of attribution methods is more faithful.

H EXTENDED TABLE FOR TABLE 2

Compared to the Table 2 in the main text, we have added the results of AUPR-In here.

I ADDITIONAL EXPERIMENTS COMPARISON WITH PRIOR OOD-AWARE METHODS

In addition to the experiments reported in the main paper, we conducted supplementary evaluations to further validate the effectiveness of FUD against recent attribution evaluation protocols such as IDSDS (Hesse et al., 2024), ROAD (Rong et al., 2022), Distill baselines (Sturmfels et al., 2020), and Gevaert et al. (2024). The results reinforce that FUD consistently produces in-distribution, high-fidelity transitional samples and more faithful attribution evaluations.

Table 8: OOD detection performance for intermediate evaluation samples (higher values indicate easier detection as OOD). We report AUROC (higher means better OOD discrimination), FPR_{95} (false positive rate at 95% true positive rate), AUPR-In, and AUPR-Out for a standard OOD detector distinguishing intermediate samples (OOD) from normal validation images (ID). **Bold** highlights the values indicating the **most ID-like (hardest to detect)** samples in each case. *Note:* In this context, AUROC, AUPR-In, and AUPR-Out values approaching 0.5 indicate maximal uncertainty in distinguishing between ID and OOD samples, thus reflecting increased in-distribution similarity and greater detection difficulty.

Model	Evaluation	AUROC ↓	FPR_{95} ↑	AUPR-In ↓	AUPR-Out ↓
RESNET-50	INS/DEL	0.8974	0.3603	0.8948	0.8893
	Sen-N	0.8773	0.5450	0.8579	0.8864
	INFID	0.7801	0.7720	0.7526	0.7876
	FUD (Ours)	0.6863	0.8317	0.6660	0.6922
ViT-B/16	INS/DEL	0.8784	0.4761	0.8529	0.8894
	Sen-N	0.8781	0.5660	0.8568	0.8734
	INFID	0.8181	0.7390	0.7904	0.8119
	FUD (Ours)	0.6450	0.9404	0.5827	0.6812

I.1 PERCEPTUAL AND STRUCTURAL FIDELITY

Table 9 compares image quality metrics of transitional samples generated by different evaluation schemes. FUD achieves the best performance across nearly all metrics, indicating that its generated samples remain both perceptually and structurally closer to the natural data distribution.

Table 9: Additional perceptual/structural fidelity results. Higher values are better for PSNR/SSIM/MS-SSIM/FSIM/HaarPSI/VSI, lower is better for GMSD.

Evaluation	PSNR ↑	SSIM ↑	MS-SSIM ↑	FSIM ↑	GMSD ↓	HaarPSI ↑	VSI ↑
IDSDES Hesse et al. (2024)	10.592	0.487	0.459	0.699	0.323	0.263	0.864
ROAD Rong et al. (2022)	18.169	0.385	0.783	0.728	0.159	0.594	0.868
Distill Sturmfels et al. (2020)	16.273	0.385	0.631	0.683	0.227	0.465	0.853
Gevaert Gevaert et al. (2024)	23.829	0.722	0.859	0.805	0.161	0.620	0.936
FUD (Ours)	25.200	0.750	0.780	0.860	0.124	0.663	0.946

I.2 OOD DETECTION ROBUSTNESS

Table 11 reports the ability of a standard OOD detector to distinguish transitional samples from true in-distribution (ID) data. Lower AUROC, AUPR-In, and AUPR-Out, and higher $FPR@95TPR$ indicate samples are harder to detect as OOD (i.e., closer to ID). FUD consistently yields the most ID-like samples across both ResNet-50 and ViT-B/16.

I.3 ADDITIONAL RUNTIME ANALYSIS OF DDIM SAMPLING

To complement the perturbation analysis in this appendix, we also report the wall-clock runtime of the DDIM sampler on ViT-B/16 for different numbers of diffusion steps. As shown in Table 10, the cost grows approximately linearly with the number of steps: increasing from 10 to 100 steps raises the per-image runtime from about 0.40s to 4.04s. Importantly, these timings correspond to the *end-to-end evaluation* of a single image-attribution pair at the given step count, i.e., they already include the full DDIM-based perturbation process along the deletion trajectory. In our experiments we use 100 steps to obtain stable in-distribution samples, but smaller step counts (e.g., 40–60) already keep the overhead within a few seconds per image, indicating that FUD remains computationally manageable for attribution evaluation.

J L2 DISTANCE BETWEEN PERTURBED AND ORIGINAL IMAGES

Table 10: Runtime of the DDIM sampler with different numbers of diffusion steps on ViT-B/16. The numbers report average wall-clock time per image (batch size 1), including the time to apply all corresponding perturbation steps.

DDIM steps	10	20	30	40	50	60	70	80	90	100
Time (s)	0.395	0.804	1.210	1.620	2.010	2.430	2.820	3.225	3.615	4.041

Table 11: Additional OOD detection results of intermediate samples.

Model	Evaluation	AUROC ↓	FPR@95TPR ↑	AUPR-In ↓	AUPR-Out ↓
ResNet-50	IDS DS Hesse et al. (2024)	0.8016	0.5653	0.7907	0.7965
	ROAD Rong et al. (2022)	0.7123	0.8226	0.6838	0.7210
	Distill Sturmfels et al. (2020)	0.8226	0.5837	0.8107	0.8178
	Gevaert Gevaert et al. (2024)	0.7690	0.6552	0.7585	0.7603
	FUD (Ours)	0.6863	0.8317	0.6660	0.6922
ViT-B/16	IDS DS Hesse et al. (2024)	0.8329	0.5803	0.8059	0.8358
	ROAD Rong et al. (2022)	0.7584	0.8000	0.7209	0.7505
	Distill Sturmfels et al. (2020)	0.8174	0.6795	0.7828	0.8255
	Gevaert Gevaert et al. (2024)	0.6675	0.9024	0.6201	0.7013
	FUD (Ours)	0.6450	0.9404	0.5827	0.6812

To quantify how strongly our diffusion-based perturbation modifies the input, we measure the pixel-wise L_2 distance between the perturbed images and the original image x .

First, for a fixed mask ratio of 10%, we track the distance between the intermediate denoised samples x_t and the original image x over the diffusion steps. As shown in Fig. 5, the mean $L_2(x_t, x)$ starts around 80 at the initial noisy state and decreases smoothly and monotonically as the diffusion proceeds, reaching values below 5 after 100 denoising steps. The shaded band indicates one standard deviation across the evaluation set. This confirms that the optimisation gradually *reduces* the perturbation while driving the samples back toward the data manifold, instead of introducing additional distortion.

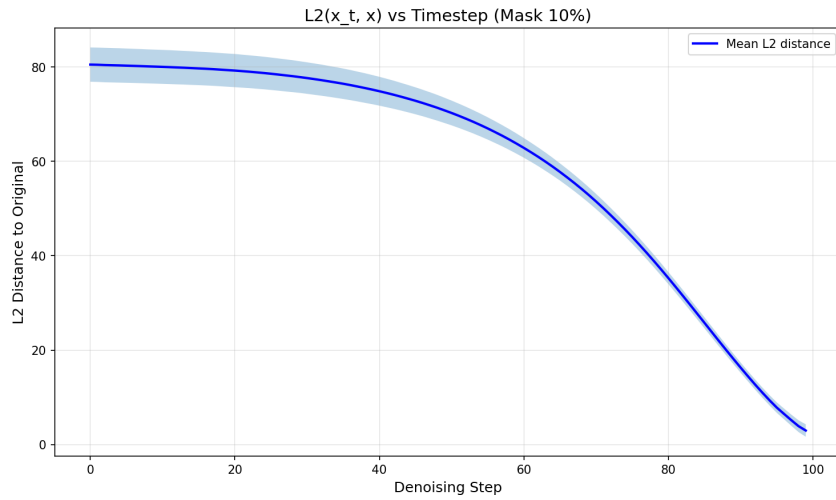
Second, we measure the final distance between the reconstructed image x_0 and the original image x for different mask ratios. Figure 6 reports the mean $L_2(x_0, x)$ as a function of the mask ratio. The distance grows approximately monotonically with the amount of masked area: it remains small for mask ratios around 10–30%, becomes moderate for 40–60%, and only becomes large when 70–90% of the image is removed. This shows that in the mask regimes typically used for attribution evaluation, our method perturbs the image relatively mildly, and stronger deviations occur only when a substantial portion of the content is intentionally removed.

K ADDITIONAL ANALYSIS OF PERTURBATION MAGNITUDE

L NOTATION SUMMARY FOR FUD

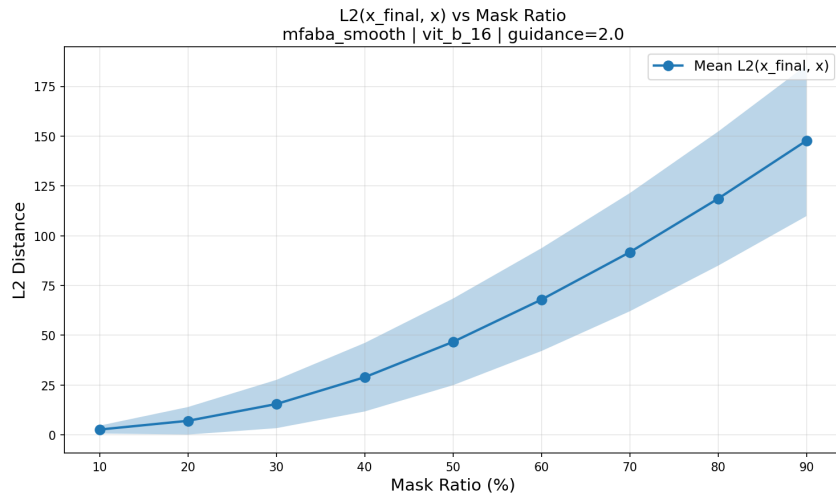
For clarity, we summarise the main symbols used in Section 3.3 (Faithfulness Under the Distribution) in Table 12. All symbols follow the notation used in the main text.

1242
1243
1244
1245
1246
1247
1248
1249
1250
1251
1252
1253
1254
1255
1256
1257
1258



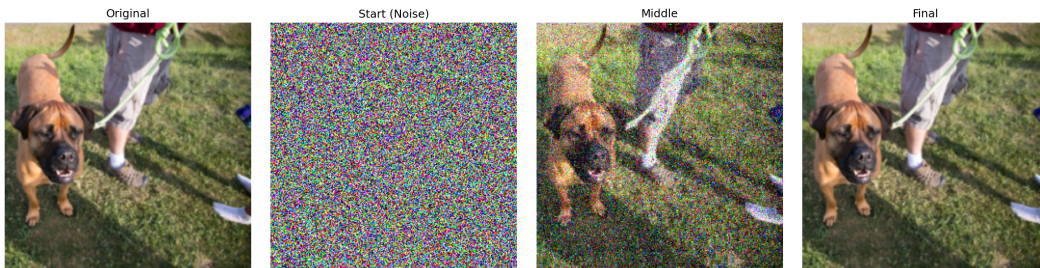
1259 Figure 5: $L_2(x_t, x)$ as a function of the denoising step for a fixed mask ratio of 10%. The solid
1260 curve shows the mean distance across images; the shaded region indicates ± 1 standard deviation.
1261

1262
1263
1264
1265
1266
1267
1268
1269
1270
1271
1272
1273
1274
1275
1276
1277
1278



1279 Figure 6: Final $L_2(x_0, x)$ after diffusion as a function of the mask ratio. We report the mean distance
1280 across images, with a shaded band for ± 1 standard deviation.
1281

1282
1283
1284
1285
1286
1287
1288
1289
1290
1291
1292
1293
1294
1295



1292 Figure 7: Qualitative “Original–Start (Noise)–Middle–Final” visualisation of the FUD denoising
1293 trajectory. From left to right: the original image x , the noisy masked starting point x_T , an
1294 intermediate denoising state x_t , and the final in-distribution sample x_0 . The final image remains
1295 visually close to the original while the masked region is restored using the diffusion prior.

1296
1297
1298
1299
1300
1301
1302
1303
1304
1305
1306
1307
1308
1309
1310
1311
1312
1313
1314
1315
1316
1317
1318
1319
1320
1321
1322
1323
1324
1325
1326
1327
1328
1329
1330
1331
1332
1333
1334
1335
1336
1337
1338
1339
1340
1341
1342
1343
1344
1345
1346
1347
1348
1349

Table 12: Summary of notation used in the definition and derivation of FUD.

Symbol	Description
x	Original input image.
\tilde{x}	Masked image constructed from x using the deletion mask M (e.g., $\tilde{x} = M \odot x + (1 - M) \odot 0$).
x^t	Intermediate sample at diffusion step t in the DDIM sampling process.
x^0	Final in-distribution evaluation sample used for the deletion trajectory (Algorithm 1 output).
y	Class label predicted by the classifier.
f	Classifier under evaluation (e.g., ViT-B/16).
M	Binary deletion mask (1 = preserve pixel, 0 = mask pixel).
$A(x)$	Attribution (saliency) map for input x used to construct the deletion masks.
$P(y x^t)$	Predictive distribution of the classifier at state x^t .
$\tilde{P}(y x^t)$	Auxiliary distribution with gradient $\nabla_{x^t} \tilde{P}(y x^t) = -\nabla_{x^t} P(y x^t)$.
z	Event encoding “no additional class- y evidence” (used in Eq. (1)).
$P(x^t z, \tilde{x}, M)$	Target conditional distribution that FUD aims to approximate.
$P(x^t)$	Unconditional image prior at step t , approximated by the score network $s_\theta(x^t)$.
$P(\tilde{x} x^t, M)$	Likelihood term enforcing consistency with the observed (unmasked) pixels.
$P(z x^t)$	Term encoding the “no new evidence for class y ” constraint.
$s_\theta(x^t)$	Learned score network approximating $\nabla_{x^t} \log P(x^t)$ (used in Eq. 6).
$S_\theta(x, \varepsilon, t)$	Score function of the DDIM sampler used in Algorithm 1.
T	Total number of DDIM sampling steps.
O	Out-of-distribution <i>threshold</i> on the diffusion time axis.
$\bar{\alpha}_t$	Cumulative noise-schedule coefficient at diffusion step t .
$\text{FUD}(f, A)$	FUD score of classifier f under attribution map A .